In-situ synthesis of NiS_2 nanoparticles/MoS_2 nanosheets hierarchical sphere anchored on reduced graphene oxide for enhanced electrocatalytic hydrogen evolution reaction

Sayyar Ali Shah,[a,#] Rani Sayyar,[a,b,#] Li Xu,[a] Hua Sun,[a] Iltaf Khan,[a] Jiyuan Guo,[b] Xiaoping Shen,[c] Shahid Hussain,[d] Aihua Yuan,[a,*] Habib Ullah,[e,*]

[a]School of Environmental & Chemical Engineering Jiangsu University of Science and Technology Zhenjiang 212100, PR China

[b]School of Science, Jiangsu University of Science and Technology, Zhenjiang, 212100, China

[c]School of Environmental & Chemical Engineering Jiangsu University of Science and Technology Zhenjiang 212003, PR China

[d]School of Materials Science and Engineering, Jiangsu University, Zhenjiang 212013, China

[e]Renewable Energy Group, College of Engineering, Mathematics and Physical Sciences, University of Exeter, Penryn Campus, Penryn, Cornwall TR10 9FE, United Kingdom

[#]Contributed Equally

Abstract

As an important energy storage and transportation carrier, hydrogen has the advantages of high combustion heat, non-toxic, and pollution-free energy conversion process. Bimetallic sulfide composites are one of the emerging catalysts for hydrogen evolution reactions (HER) during water splitting. Herein, a hydrothermal method has been employed for the in-situ synthesis of NiS_2 nanoparticles/MoS_2 nanosheets (NiS_2/MoS_2) hierarchical sphere anchored on reduced graphene oxide (RGO) for enhanced electrocatalytic HER activity. The NiS_2/MoS_2/RGO composite displays improved HER activity compared to MoS_2/RGO and NiS_2/RGO. The optimized NiS_2/MoS_2/RGO-9 requires only an overpotential of 136 mV at a current density of 10 mA cm^{-2}, a small Tafel slope of 53.4 mV $dec^{-1,}$ and good stability in acid solution. The synergetic effect between NiS_2 nanoparticles and MoS_2 nanosheets is responsible for enhanced HER performance. Moreover, RGO provides the substrate for NiS_2/MoS_2 species and maintains the overall conductivity of NiS_2/MoS_2/RGO composites. Finally, density functional theory (DFT) calculations justify and approve the efficient HER activity of NiS_2/MoS_2/RGO in terms of lower Gibbs free energy (0.07 eV) and lower work function (3.98 eV) that subsequently enhance the dissociation of H_2O.

Keywords: Hydrogen evolution reaction, hydrothermal method, NiS_2/MoS_2/RGO composite, synergetic effect, density functional theory

1. Introduction

With the development of the economy and technology, the rapid consumption of energy sources and the decline of environmental quality have become increasingly serious issues [1]. The development of sustainable green energy is urgently needed for modern society. As an ideal secondary energy source, hydrogen energy has the advantages of high efficiency, zero pollution, and sustainability [2,3]. The electrochemical water splitting is an ideal strategy for green H_2 production [4-6]. However, sluggish HER kinetics in water splitting process required an active catalyst to drive the hydrogen evolution reaction (HER) at low overpotential. Platinum or Platinum based materials are the most effective electrocatalyst for HER [7]. However, Platinum is scarce and expensive, which limits its use in industrial applications. Therefore, attention has been paid to for searching sustainable and low-cost catalysts to replace precious metal catalysts to realize the production of hydrogen energy [8-18].

In the past decades, MoS_2 has attracted huge attention for electrocatalytic HER due to its unique properties [19,20]. MoS_2 has a layered material and has rich catalytic active sites at the edge for HER activity [21-23]. However, its MoS_2 is a semiconductor material and exhibits relatively poor catalytic activity for HER. To improve the HER catalytic activity of MoS_2, many attempts such as doping of heteroatoms, basal plane activation, expanded interlayer spacing, hierarchical morphology, defects, and disorder engineering have been made [24-29]. However, the HER performance of MoS_2 still does not reach to benchmark.

The MoS_2-based composites, especially bimetallic sulfides emerged as a promising candidate for improved HER performance [30-32]. The heterostructure interface engineering of MoS_2 with other metallic sulfides creates more catalytic active sites on interfaces for

enhanced HER catalytic activity due to the strong synergy between the two different phases [9,33]. Furthermore, the interaction between different metallic sulfide phases at a heterogeneous interface alters electrons distribution and facilitates a moderate Gibbs free energy for proton, which leads to improved HER catalytic activity of composites [34]. Recently, the NiS_2/MoS_2 heterojunction composite exhibits good HER performance and durability. For example, Kuang et al. prepared NiS_2/MoS_2 hybrid nanowires by in situ chemical vapor deposition process and display good HER performance in acidic, alkaline, and neutral conditions [34]. The HER catalytic activity of bimetallic sulfides can be further enhanced by improving electrical conductivity. The NiS_2/MoS_2 composites combined with high conductive materials, especially graphene, carbon nanotube, and carbon cloth can promote electrocatalytic activity for HER.[35-38] Mao *et al.* synthesized NiS_2-MoS_2 on polymer/graphene oxide by a hydrothermal method and shows excellent HER activity with an overpotential of 205 mV at a current density of 10 mA cm^{-2} and good stability in acidic conditions [35]. Wang *et al.* reported a tree-like NiS_2/MoS_2-RGO nanocomposite that exhibits good HER performance over a wide range of pH [36]. Zheng *et al.* prepared Co-doped MoS_2/NiS_2 nanosheet array on the carbon cloth substrate by three-step hydrothermal processes for enhanced HER activity [37]. Li and a co-worker reported Fe-doped NiS_2-MoS_2/carbon nanotube hybrid as an electrocatalyst for outstanding HER activity with good stability in acidic solution.[38] Some efforts have been made to obtain NiS_2/MoS_2 composites for improved electrochemical HER activity. The in-situ interface engineering strategy for the synthesis of NiS_2 nanoparticles/MoS_2 nanosheets on a conductive substrate is rarely reported for enhanced HER activity.

Here, we used a hydrothermal method for in-situ preparation of NiS_2 nanoparticles/MoS_2

nanosheets hierarchical sphere anchored on the RGO (NiS_2/MoS_2@RGO) as an efficient electrocatalyst for HER. NiS_2 nanoparticles are selectively decorated on MoS_2 nanosheets in NiS_2/MoS_2@RGO composites. The optimal NiS_2/MoS_2@RGO-9 sample displays excellent HER performance and good stability in 0.5 M H_2SO_4 solution. The improved HER performance of NiS_2/MoS_2@RGO composites due to the synergistic effect between NiS_2 nanoparticles and MoS_2 nanosheets and RGO provides the conductive channel and substrate for NiS_2/MoS_2 sphere. Finally, theoretical calculations were performed to countercheck the efficient HER activity of our experimentally observed NiS_2/MoS_2/RGO. Gibbs's free energy, the partial density of states (PDOS), and electron difference density (EDD) are simulated to validate and confirm the performance of the reported catalyst.

2. Experimental section

2.1 Synthesis of GO

The graphene oxide (GO) was synthesized as reported by the Hummers method with some modifications [39,40].

2.2 Synthesis of $Mo_3O_{10}(C_2H_{10}N_2)$ rods

The $Mo_3O_{10}(C_2H_{10}N_2)$ rods were prepared according to the previous report [41]. Briefly, $(NH_4)_6Mo_7O_{24}\cdot 4H_2O$ (0.1 g) stir vigorously in 15 mL water for 30 minutes. Then $C_2H_4(NH_2)_2$ (0.85 mL) was poured into the reaction mixture and subsequently dropwise HCl (0.5 M) was added to it until the pH value approximately reached 4.5. This reaction mixture was heated at 50 °C with continued stirring for 2 hours in a water bath. The obtained ethylenediamine trimolybdate ($Mo_3O_{10}(C_2H_{10}N_2)$) rods were washed and dried.

2.3 Synthesis of NiS_2/MoS_2/RGO composite

The GO (50 mg) nanosheets were dispersed in water (15 mL) by sonication. The L-cysteine (0.28 g) was added and sonicated to completely dissolve it in GO dispersion. This was followed by the addition of $Mo_3O_{10}(C_2H_{10}N_2)$ rods (100 mg) to the reaction mixture and sonication for another 1 h. Then nickel nitrate (90 mg) was dissolved in aqueous dispersion for 30 min. A Teflon-lined stainless-steel autoclave (25 mL) containing the reaction mixture was heated at 200 °C for 14 h. The products were obtained by centrifugation and washed four times with water and ethanol, respectively. Before use, the product was dried at 50 ˚C for 15 h in a vacuum oven. The other samples using different amounts (10, 50, 130, and 170 mg) of nickel nitrate were prepared by the same procedure (Table S1).

2.4 Synthesis of MoS_2/RGO, NiS_2/ RGO and NiS_2/MoS_2

MoS_2/RGO and NiS_2/ RGO composites were prepared by the same hydrothermal method. The GO (50 mg), L-cysteine (0.28 g), and $Mo_3O_{10}(C_2H_{10}N_2)$ rods (100 mg) were taken as a reaction mixture for the synthesis of MoS_2/RGO, while GO (50 mg), L-cysteine (0.28 g), and nickel nitrate (90 mg) were used as initial precursors for the synthesis of NiS_2/RGO (Table S1). *The* NiS_2/MoS_2 sample was prepared using L-cysteine (0.28 g), $Mo_3O_{10}(C_2H_{10}N_2)$ rods (100 mg), and nickel nitrate (90 mg) in the same conditions.

2.5 Microstructure characterization

The crystal phases of the obtained samples were characterized using an X-ray powder diffractometer (Shimadzu XRD-6000). The morphologies and structures of samples were examined by a scanning electron microscope (SEM, FEI 250) and a high-resolution

transmission electron microscope (HRTEM, JEOL JEM-2100F). The elemental mapping images were scanned by energy dispersive X-ray spectroscopes attached to TEM. Raman scattering spectrum was conducted using Renishaw invia Confocal Raman Microscope at room temperature. X-ray photoelectron spectra (XPS) were obtained using a fully integrated X-ray photoelectron spectroscope (Thermo Scientific Nexsa).

2.6 Electrochemical measurements

We performed electrochemical tests by an electrochemical workstation (CHI 760E) of a typical three-electrode cell. Glassy carbon, graphite rod, and saturated calomel electrode (SCE), were used as the working, counter, and reference electrodes, respectively. Catalyst (4 mg) and Nafion solution (30 μL, 5 wt%) were sonicated in a mixture of absolute ethanol (370 μL) and deionized water (600 μL) to obtain homogenous ink. The ink (5 μL) was loaded on a glassy carbon electrode and kept in the open air for drying. The cyclic voltammogram (CV) was performed for 50 cycles between 0 -0.7 V *vs*. SEC before linear sweep voltammetry (LSV). LSV curves were measured at a scan rate of 5 mV s^{-1} in 0.5 M H_2SO_4 solution. To evaluate the electrochemically active surface area (EASA) of the catalysts, the double-layer capacitance (C_{dl}) was obtained by measuring the CV between the 0-0.1 V *vs*. SCE at different scans rates (10-100 mV s^{-1}). Electrochemical impedance spectroscopy (EIS) tests were carried out from 100 kHz to 0.01Hz frequency range in the same condition. The stability of the catalyst was measured for 1000 and 2500 CV cycles at a scan rate of 100 mV s^{-1} between 0 and -0.7 V *vs*. SCE. The LSV curves of the catalyst after 1000 and 2500 CV cycles were again measured. The amperometric (i-t) curve was also obtained to further confirm the stability of our sample.

2.7 Computational methodology

Ab initio DFT calculations were performed for the as-prepared electrocatalysts, using Quantum ATK [42]. The results were examined on vnl Version 2019.12 and VESTA software [43]. In order to represent the observed NiS_2/MoS_2 heterostructure, first we model (i) NiS_2 nanoparticle (ii) then a single layer of MoS_2 sheet, (iii) followed by the adsorption of MoS_2 on NiS_2 to make NiS_2/MoS_2 heterojunction, which is shown in Fig. S1.

The HER activity of NiS_2, MoS_2, and NiS_2/MoS_2 was calculated from the Gibbs free energy (ΔG_{H*}). In this case, we attached one H atom to the surface of these species and the systems were allowed to be relaxed. The size of our theoretical model is smaller compared to that of our experimental catalyst. However, the important influence on the electronic property can be described from the above-mentioned models. Pure DFT method such as GGA with exchange-correlation functional of PBE at double Zeta Polarized (DZP) basis set is utilized for the energy and structural optimization. As discussed elsewhere, the LCAO method has been chosen for Ni, Mo, S, and H atoms [44]. A 7×7×3 Monkhorst-Pack k-point sampling is utilized for the optimization and 7x7x7 for the electronic property simulations.

As we previously reported [45], the overall HER mechanism of an electrocatalyst can be estimated from a three-state diagram. This diagram is consist of (i) an H^+ state, (ii) an excited intermediate H*, and (iii) a $1/2H_2$ state. As we know, the free energy of H* (ΔG_{H*}) is crucial to expressing the HER performance of an electrocatalyst. The positive value ΔG_H of an electrocatalyst shows little kinetics for hydrogen adsorption. While the negative ΔG_{H*} describes the low kinetics for the release of an H_2. So, the acceptable ΔG_{H*} must be close to 0;

i.e., the ΔG_{H*} value of a PGM-based catalyst such as Pt is near-zero as $\Delta G_{H*} \approx 0.09$ eV [46]. In this work, we have simulated the ΔG_{H*} with the help of Equation (1).

$$\Delta G_{H*} = \Delta E_{H*} + \Delta E_{ZPE} - T\Delta S_H \quad (1)$$

In Equation (1), ΔE denotes the total energy change which can be simulated from the free energy DFT, ΔE_{ZPE} and ΔS are the differences in zero-point energy and entropy, respectively. While T describes the ambient temperature (298.15 K). The free energies of the elementary reactions vary along with the change in pH, so, here the theoretical working potential is independent of pH. In this case, the possible controlling step remains constant. We have simplified theoretical data by setting the pH=0. The STP hydrogen-free energy can be obtained from the energy of $1/2H_2$. Finally, the entropy of H_2 is obtained from the NIST database [47].

$$\Delta E_{H*} = E_{(H*)} - E_{(*)} - 1/2E_{H_2} \quad (2)$$

In Equation (2), $E_{(H*)}$ and $E_{(*)}$ are the energy of the given surface with and without H adsorption, calculated from the DFT. The E_{H_2} is the gas phase calculated energy of H_2. The ΔE_{H*} is the interaction energy of hydrogen over the surface of the catalyst. Eq. (1) can be amended as follow.

$$\Delta G_{H*} = \Delta E_{H*} + 0.37 \text{ eV} \quad (3)$$

So, we calculate the free energy of H with the help of Equation 3.

3. Results and discussion

3.1 Preparation and characterizations

The preparation process of the products is shown in Scheme 1. The L-cysteine,

$Mo_3O_{10}(C_2H_{10}N_2)$ rod, and $Ni(NO_3)_2$ were added to an aqueous dispersion of GO nanosheets and subsequently heated to 200 ˚C for 14 h. In hydrothermal conditions, the S species of L-cysteine bonded to oxygen-containing functional groups (active sites) of GO nanosheets, which are crystal seeds for nucleation of MoS_2 nanosheets.[48] $Mo_3O_{10}(C_2H_{10}N_2)$ rods dissociate into $Mo_3O_{10}^{2-}$ anions and ethylenediamine species at elevated temperature and $Ni(NO_3)_2$ into Ni^{2+} and $(NO_3)^{1-}$ ions. The $Mo_3O_{10}^{2-}$ anions react to S to generate MoS_2 nanosheets[49], and meanwhile, Ni^{2+} ions also react with some S to form NiS_2 nanoparticles. The MoS_2 grows in hierarchical sphere nanosheets, possibly due to intrinsic layered crystal structure and van der Waals forces. The NiS_2 nanoparticles are selectively loaded on MoS_2 nanosheets because of the presence of a common S cation. During the hydrothermal condition, GO nanosheets were reduced to RGO. As a result, the NiS_2/MoS_2 hierarchical sphere is anchored on RGO to form NiS_2/MoS_2@RGO hybrid electrocatalyst.

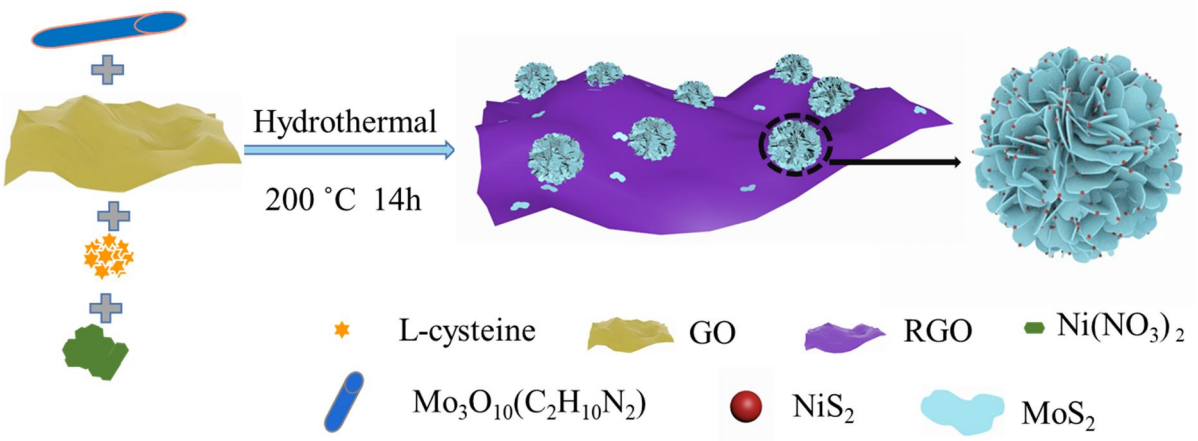

Scheme 1. Illustration of synthetic process of NiS_2/MoS_2/RGO composites.

The XRD pattern and SEM images of the $Mo_3O_{10}(C_2H_{10}N_2)$) rods are reported in our previous report [45]. The XRD pattern of samples is shown in Fig. 1a. The XRD pattern of as-

prepared MoS_2/RGO composite displays peaks at about 8.8°, 32.5°, and 57.8°, which can be related to (002), (100), and (110) crystallographic planes of hexagonal 2H-MoS_2 (JCPDS card No. 37-1492), respectively. The peak of as-prepared MoS_2 nanosheets shifted from 14.4° to a lower angle of about 8.9° compared to the bulk MoS_2. It suggests expanding the interlayer spacing of as-prepared MoS_2 nanosheets. NiS_2/RGO sample show peaks at 31.3°, 35.2°, 38.6°, 45.1°, 53.4°, 58.5°, and 61.0°, which can be assigned to (200), (210), (211), (220), (311), (023), and (321) crystallographic planes of cubic NiS_2 (JCPDS, No. 65-3325), respectively. The composites show the diffraction peaks for the mixture of NiS_2, MoS_2 nanosheets, and carbon. The characteristic peaks shown at 2θ are approximately 31.3°, 35.2°, 45.1°, and 53.5°, especially when high concertation $Ni(NO_3)_2$ salt added reaction mixture can be obviously seen. It clearly indicates the increase of $Ni(NO_3)_2$ precursor more NiS_2 nanoparticles formed. The obvious diffraction peak observed at 8.8° composites indicates the formation of (002) crystal plane of MoS_2 nanosheets and is well consistent with the MoS_2/RGO simple. It suggests that the composites containing MoS_2 nanosheets also show the interlayer spacing of MoS_2 nanosheets. Expanding the interlayer spacing of MoS_2 nanosheets may be the incorporation of chemical species during the hydrothermal process [50]. A broad peak centered at 2θ values about 24° in all samples can be related to the (002) reflection of graphitic carbon and demonstrated graphene oxide is reduced to RGO in hydrothermal conditions.

The Raman spectrum was measured as shown in Fig. 1b. The D and G bands at 1347 and 1590 cm^{-1} indicate the presence of RGO in composite, respectively. The I_D/I_G ratio is about 0.9, which suggests a good graphitization of the RGO [49]. The relative weak peaks (enlarged and shown in the inset of Fig. 1b) at 404 cm^{-1} correspond to in-plane optical vibration mode (E^1_{2g})

and 375 cm^{-1} out-of-plane optical vibrations (A^1_g) of MoS_2 nanosheets [48,49]. Raman spectrum is very useful to determine the number of layers of MoS_2 from frequency difference (Δk) [51]. The Δk of MoS_2 nanosheets in the samples is 29 cm^{-1} and suggested a few layers of MoS_2 nanosheets during the synthesis process. The peaks are approximately 298 and 347 cm^{-1} which can be associated with the Ni-S mode of NiS_2 [52,53].

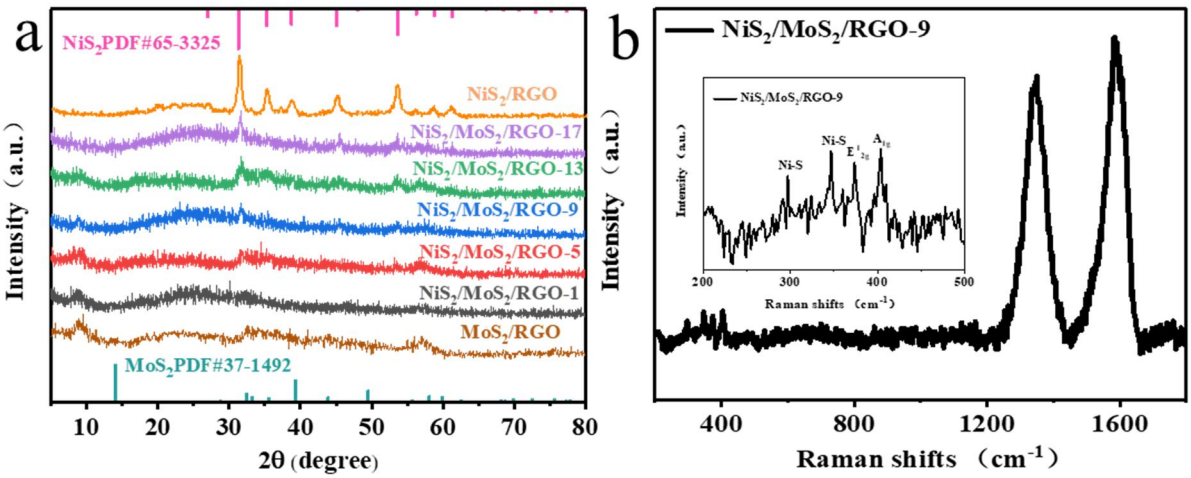

Fig. 1. (a) XRD patterns of obtained as-prepared samples. (b) Raman spectrum of NiS_2/MoS_2/RGO-9 composite.

The SEM images of NiS_2/MoS_2/RGO-9 are shown in Fig. 2. We can see randomly distributed spheres anchored on RGO (Fig. 2a). The area of the RGO is tens of micrometers and sizes spheres ranging from tens of nanometers to hundreds of nanometers. The morphology of the spheres is hierarchical and composed of layered types of structure (Fig. 2b).

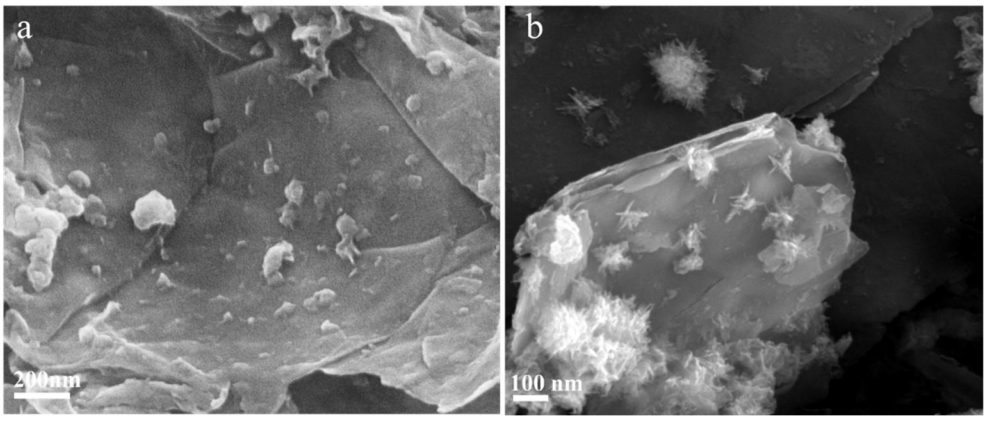

Fig. 2. (a,b) SEM images of the NiS_2/MoS_2/RGO-9.

The TEM images of NiS_2/MoS_2/RGO-9 sample are shown in Fig. 3a-c. The hierarchical sphere with sizes from nanometer to micrometers anchored on RGO can be observed (Fig. 3a). On high magnification TEM images, it is clearly seen that the hierarchical sphere is contained of nanoparticles and nanosheets-like structures (Fig. 3b,c). The nanoparticles cannot be observed without a hierarchical sphere, suggesting strong interaction of hierarchical nanosheets and nanoparticles. The nanoparticles are very small and the average size is about 20 nm. The MoS_2 nanosheets distributed on RGO of MoS_2/RGO sample as shown in TEM images of Fig. S2a,b, while only aggregated nanoparticles are observed on RGO of NiS_2/RGO composite (Fig. S2c,d).

The hierarchical layer structures are MoS_2 nanosheets and nanoparticles are NiS_2 of NiS_2/MoS_2/RGO-9 sample confirmed by HRTEM (Fig. 3d,e). The HRTEM image shows zigzag lamellar structures, which are (002) crystal planes of MoS_2 nanosheets. The interlayer spacing of MoS_2 nanosheets is about 0.76-0.92 nm and this interlayer spacing of MoS_2 nanosheets expanded compared to bulk MoS_2 [23,26]. The lattice fringes of nanoparticles are about 0.28 nm and match with the (200) crystal plane of NiS_2. The HRTEM images of NiS_2

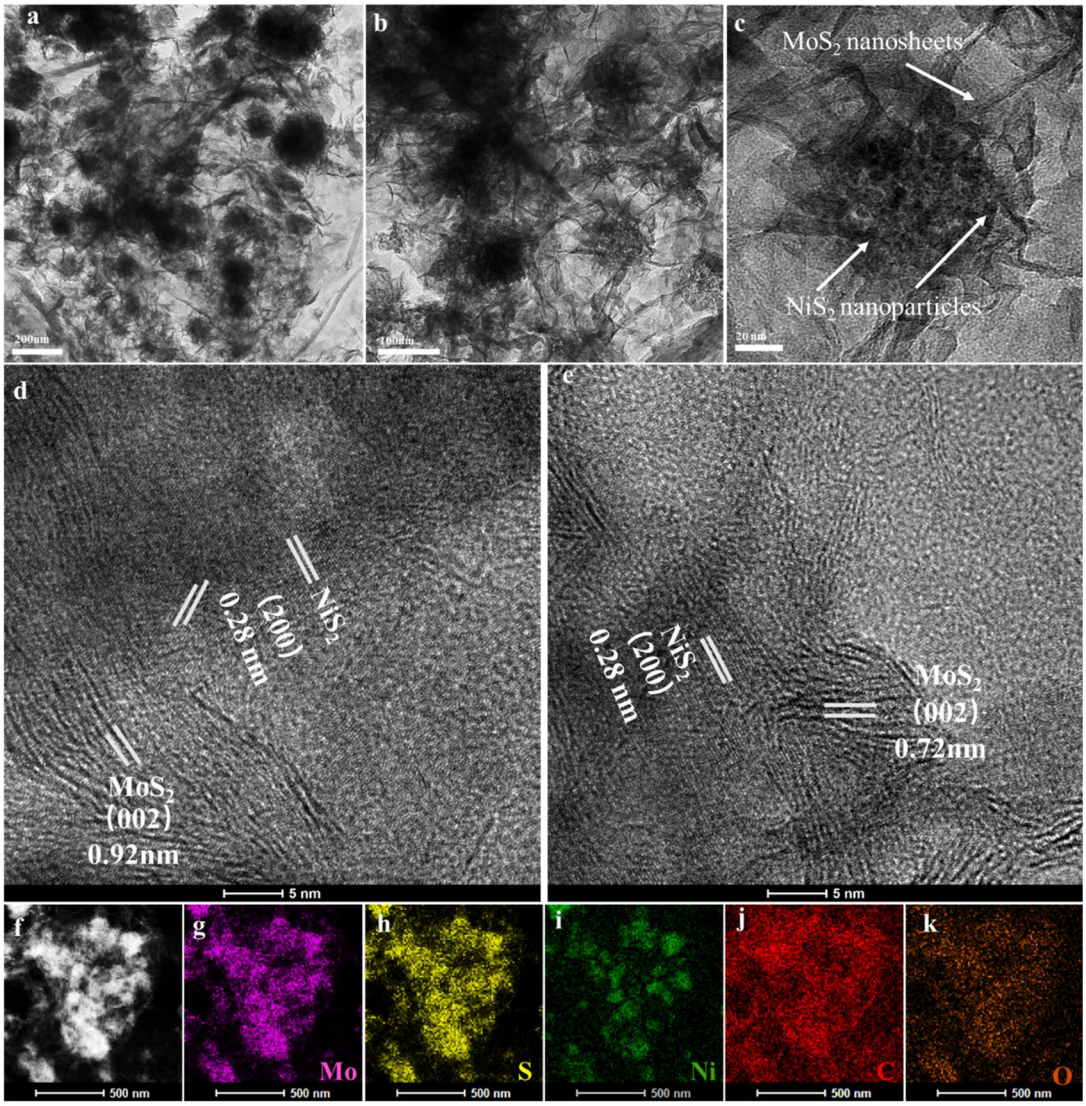

Fig. 3. (a-c) TEM images of the NiS_2/MoS_2/RGO-9 composite. (d-e) HRTEM images of the NiS_2/MoS_2/RGO-9 composite. (f) Dark-field TEM image of the NiS_2/MoS_2/RGO-9 (g-k) and their corresponding EMI of (g) Mo, (h) S (i), Ni (j), C, and (k) O.

nanoparticles and MoS_2 nanosheets product clearly show heterostructure and amounts of heterointerfaces. The obvious heterointerfaces engineering between NiS_2 nanoparticles and MoS_2 nanosheets can alter the electronic structure elements at interfaces and enhanced catalytic performance [34]. Furthermore, MoS_2 nanosheets with expanded interlayer spacing and hierarchical morphology can assist to enhance the HER performance [27,50]. Fig. 3f shows

the dark fields TEM image and Fig. 3g-k represents corresponding elemental mapping images (EMI) of NiS_2/MoS_2/RGO composite. The signals of Mo, S, and Ni are non-homogenous in EMI and obvious where hierarchical spheres are formed. The carbon is relatively weak and homogenous and incites that NiS_2/MoS_2 hierarchical spheres anchored on RGO, while O signal rises from RGO and surfaces oxidation of composites.

The element chemical states of as-prepared samples were examined by XPS analysis. The survey XPS spectra show that NiS_2/MoS_2/RGO-9 composite contains Mo, Ni, S, C, and O elements, while Mo and Ni peaks are not observed in NiS_2/RGO and MoS_2/RGO composites, respectively (Fig. S3). The Mo 3d orbital XPS spectrum of NiS_2/MoS_2/RGO-9 and MoS_2/RGO composites can be fitted into different peaks (Fig. 4a). The strong peaks at approximately 231.3 eV and 228.2 eV of NiS_2/MoS_2/RGO-9 correspond to Mo $3d_{5/2}$ and Mo $3d_{3/2}$ of the Mo^{4+} valence state, respectively, and indicate the presence of MoS_2.[42,47] These peaks are slightly shifted towards high binding in the MoS_2/RGO composite. The other peaks at 235.5 and 232.5 eV can be associated with the Mo^{6+} valance state of Mo $3d_{5/2}$ and Mo $3d_{3/2}$ spin-orbit doublet, respectively [45,50] and suggest surface oxidation of MoS_2 nanosheets. A relatively small peak at 225.5 eV is ascribed to the S 2s orbital of S [12,27]. Fig. 4b shows the Ni 2p spectra of the NiS_2/MoS_2/RGO-9 and NiS_2/RGO. The XPS spectrum Ni 2p deconvoluted into spin-orbit doublets at 854.3 and 872 eV, corresponding to the $2p_{3/2}$ and $2p_{1/2}$ of Ni^{2+}, respectively, while other peaks at 856.9 and 875.3 eV related to the $2p_{3/2}$ and $2p_{1/2}$ of Ni^{3+}, respectively [12,54,55]. The peaks observed at 860 and 878.6 eV are shakeup satellites of Ni 2p [52]. The peaks of Ni^{2+} of Ni 2p spin-orbit doublets in NiS_2/MoS_2/RGO-9 composite are slightly shifted to high binding energy and more intense compared to NiS_2/RGO sample. The shifting of Mo 3d to low binding

energy and Ni^{2+} to high binding energy in NiS_2/MoS_2/RGO-9 sample compared to MoS_2/RGO-9 and NiS_2/RGO, respectively, indicate an interaction between MoS_2 nanosheets and NiS_2 nanoparticles. The S 2p orbitals XPS spectrum would be fitted into four peaks (Fig. 4c). Possibly, the peaks at 162.2 and 164.5 eV are related to S $2p_{3/2}$ and S $2p_{1/2}$ orbitals of MoS_2, respectively [55]. The other peaks at 161.5 eV and 163.2 eV binding energy can be associated with the Ni-S bond of S $2p_{3/2}$ and S $2p_{1/2}$ bands, respectively [55]. The XPS spectrum of C 1s (Fig. 4d) shows peaks at 284.7 eV binding energy for C=C and/or C-C bonds [49]. The peaks at 285.9 eV and 288.7 eV binding energy can be attributed to C-O and C=O bonds, respectively [49].

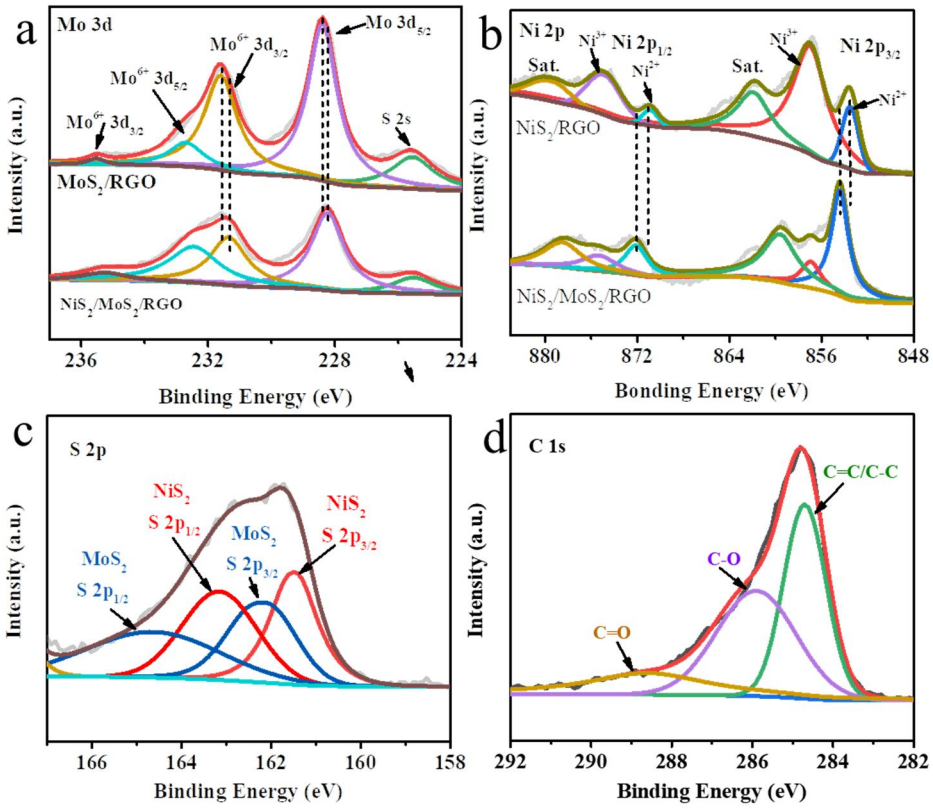

Fig. 4. XPS spectra of (a) Mo 3d, (b) Ni 2p, (c) S 2p, and (d) C 1 s (f) orbitals of NiS_2/MoS_2/RGO-9 composite.

3.2 Electrocatalytic HER performance

The as-prepared samples and 20 % Pt/C catalyst were investigated for HER performance under the same conditions. The HER performance of samples was studied in acidic solution (0.5 M H_2SO_4 M) using a three-electrode system. The LSV curves (with *iR* compensation) of the tested samples show in Fig. 5a. The commercial 20 % Pt/C catalyst displays the best HER performance with an overpotential 31 mV at a current density of 10 mA cm^{-2}. Among the as-prepared samples, NiS_2/MoS_2/RGO-9 composite showed better HER performance and required an over protentional ~136 mV to achieve 10 mA cm^{-2} and better than those of NiS_2/MoS_2/RGO-1 (198 mV), NiS_2/MoS_2/RGO-5 (165 mV), NiS_2/MoS_2/RGO-13 (212 mV), NiS_2/MoS_2/RGO-17 (220 mV), MoS_2/RGO (292 mV), NiS_2/RGO (387 mV), and NiS_2/MoS_2 (313 mV) (Table S2). All the NiS_2/MoS_2/RGO composites display better HER performance compared to NiS_2/RGO and MoS_2/RGO-17 catalysts. This suggests that the enhanced catalytic activity of NiS_2/MoS_2/RGO composites would be attributed to the synergistic effect between NiS_2 nanoparticles and MoS_2 nanosheets. Moreover, the overpotential of the physical mixture of MoS_2/RGO and NiS_2/RGO (1:1) (NiS_2/RGO-MoS_2/RGO-P) is 236 mV at a current density of 10 mA cm^{-2} and less than all MoS_2/NiS_2/RGO composites. It can be observed that NiS_2/MoS_2/RGO composites that an overpotential value at 10 mA cm^{-2} firstly decreases and then increases with the increase of NiS_2 species. The enhancement of HER performance with increasing NiS_2 phases in composites (NiS_2/MoS_2/RGO-1 and NiS_2/MoS_2/RGO-5) indicates the formation of more heterointerfaces until reached an optimal ratio (NiS_2/MoS_2/RGO-9). On further increasing of NiS_2 phases in the composites (NiS_2/MoS_2/RGO-130 and NiS_2/MoS_2/RGO-170), the HER performance decreases due to the bad conductivity of NiS_2

[56]. Our prepared NiS_2/MoS_2/RGO-9 catalyst shows better or comparable performance NiS_2/MoS_2-based catalysts (Table S3).

Furthermore, Tafel slopes were calculated from Tafel plots based on LSV curves to understand the details of HER activity. The linear portions of LSV curves were fit to in the Tafel equation (Fig. 5b). The Tafel slope of 20 % Pt/C, NiS_2/MoS_2/RGO-1, NiS_2/MoS_2/RGO-5, NiS_2/MoS_2/RGO-9, NiS_2/MoS_2/RGO-13, NiS_2/MoS_2/RGO-17, NiS_2/MoS_2, MoS_2/RGO and NiS_2/RGO are 35, 63.4, 60.7, 53.4, 69.3, 75.7, 95.3, 85.8, and 100. 2 mV dec^{-1}, respectively. The smaller the Tafel slope suggests faster the reaction kinetic and a rapid increase of HER rate with overpotential. Among the as-prepared sample, NiS_2/MoS_2/RGO-9 catalyst small Tafel slope and fast reaction kinetics. Basically, HER performed in the acidic condition required three principal steps including the Volmer, Heyrovsky, and Tafel.[29,46,57] The Tafel slope value of our best samples is 53.4 mV dec^{-1} and the HER mechanism is dominated by the Volmer-Heyrovsky reaction where electrochemical desorption is the rate-determining step.

The electrochemical surface area (ECSE) of catalysts was measured to obtain electrochemical double-layer capacitances (C_{dl}) of the composites. CV cycles were measurements at different scan rates 10-100 mV (Fig. S4a-g) in the non-Faraday region. The C_{dl} value of NiS_2/MoS_2/RGO-1, NiS_2/MoS_2/RGO-5, NiS_2/MoS_2/RGO-9, NiS_2/MoS_2/RGO-13, NiS_2/MoS_2/RGO-17, MoS_2/RGO, and NiS_2/RGO composites are 5.6, 8.22, 9.59, 5.3, 4.5, 1.9, and 0.8 mF cm^{-2}, respectively (Fig. S4h). The high C_{dl} value of NiS_2/MoS_2/RGO-9 catalyst suggests that more catalytic active sites are present on its surface which is consistent with the better catalytic performance.

The electrochemical impedance of the catalyst is measured by electrochemical impedance spectroscopy (EIS). The Nyquist plots are shown in Fig. 5c and fitted with an equivalent circuit (inset of Fig. 5c). The charge transfer resistance (R_{ct}) of NiS_2/MoS_2/RGO-1, NiS_2/MoS_2/RGO-5, NiS_2/MoS_2/RGO-9, NiS_2/MoS_2/RGO-13, NiS_2/MoS_2/RGO-17, MoS_2/RGO, and NiS_2/RGO composites are 75.6, 72, 56.6, 82.9, 93.7, 117.7, and 128.6 Ω, respectively. The lower R_{ct} value of NiS_2/MoS_2/RGO-9 compared with those of other samples indicates more effective charge transfer at the electrode/electrolyte interface for enhanced catalytic performance.

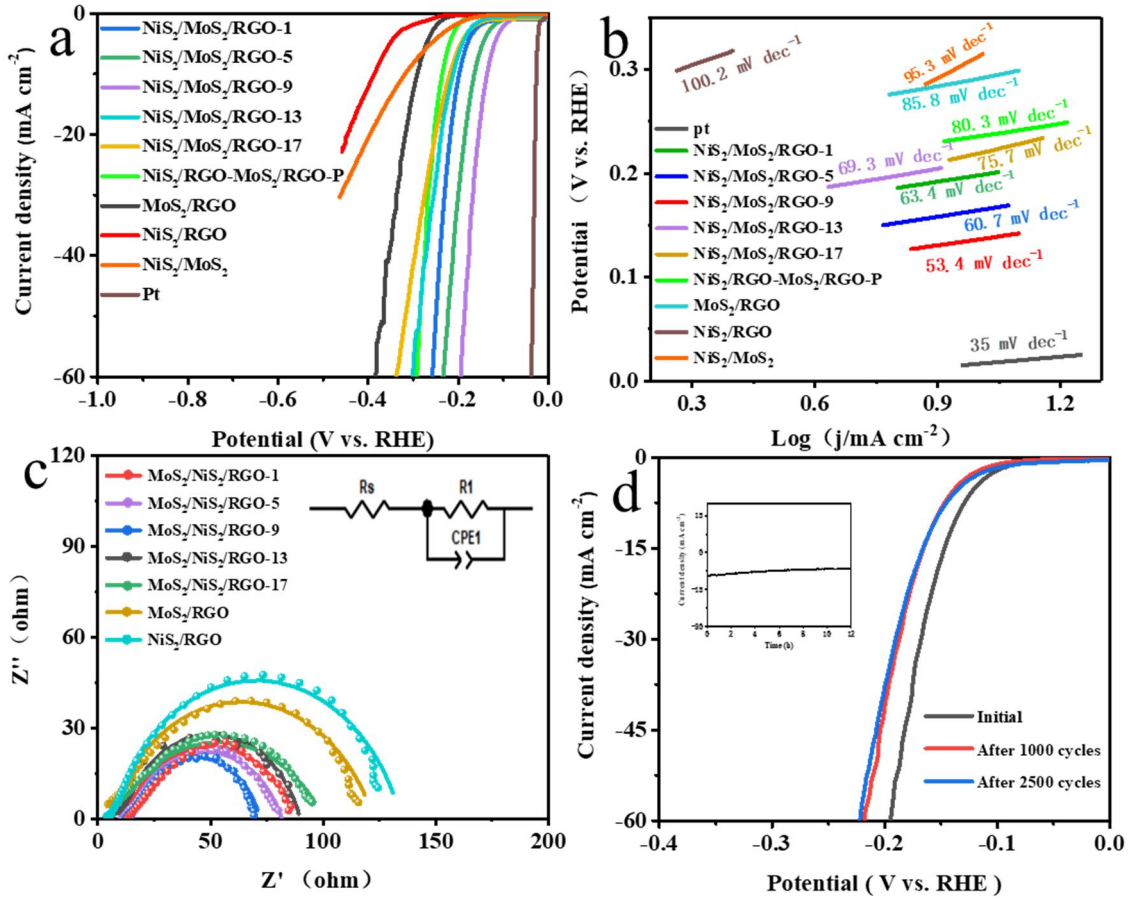

Fig. 5. (a) LSV curves of commercial 20 % Pt/C, NiS_2/RGO-MoS_2/RGO-P, and as-prepared catalysts, (b) the Tafel plots calculated from LSV curves. (c) Nyquist plots and equivalent circuit (inset of "c"), which is used for fitting the experimental data of as-prepared samples. (d) LSV curves of NiS_2/MoS_2/RGO-9 catalyst before and after 1000 and 2500 CV cycles, the

chronoamperometric curve of NiS_2/MoS_2/RGO-9 catalyst shown in the inset of "d".

Stability is another important criterion for catalyst. The stability of the NiS_2/MoS_2/RGO-9 catalyst was measured by CV cycles (Fig. 5d). The LSV curve obtained after 1000 CV cycles show a slight performance decay of NiS_2/MoS_2/RGO-9 catalyst. We also measured the LSV curve after 2500 CV cycles and it displays no further loss of HER performances. This suggests the high stability of NiS_2/MoS_2/RGO-9 catalyst. The hierarchical sphere with little modification of NiS_2/MoS_2 can be observed on the surface of RGO after 2500 CV cycles in TEM images (Fig S5), suggesting structure stability of the composite. The XPS survey spectrum of NiS_2/MoS_2/RGO-9 composite after 2500 CV cycling shows peaks for S, Ni, Mo, O, and C elements, indicating good stability of electrocatalyst (Fig. S6a). The small peak at 650 eV may be due to F 1s of the Nafion solution. The XPS spectrum Mo 3d region shows well-defined peaks for the Mo^{4+} ions indicating the stability of MoS_2 nanosheets (Fig. S6b). However, the peak intensity of Mo^{6+} ions increased, indicating the surface oxidation of MoS_2. Similarly, the XPS spectra Ni 2p and S 2s regions also oxidized during the electrochemical process (Fig. S6c,d). The XPS spectrum C 1s show no obvious change after the stability test (Fig. S6e). Furthermore, the amperometric (i-t) test (inset Fig. 5d) was also measured for 12 h to further confirmed the stability of NiS_2/MoS_2/RGO-9 composite. The difference in the initial and after 12 h current density is very small and displays the long-term durability of our product. From LSV curves before and after i-t test Fig S7, no obvious difference is observed in the HER performance.

3.3 Electronic structure properties

In order to understand the synergistic effect of the heterointerfaces of NiS_2 nanoparticles, and MoS_2 nanosheets for enhanced HER performance of NiS_2/MoS_2/RGO composites, first-principles DFT simulations were carried out. As discussed in the methodology section, the ΔG_{H^*} is calculated over the surface of NiS_2 nanoparticles, MoS_2 nanosheets, and NiS_2/MoS_2 composite (Fig. S1). A reasonable ΔG_{H^*} value is essential for an efficient electrocatalyst to lower the reaction barriers in the HER process, in the adsorption and desorption stages. The ΔG_{H^*} of the NiS_2 nanoparticles, MoS_2 nanosheets, and NiS_2/MoS_2 composite are -1.20, -0.14, and 0.07 eV, respectively (Fig. 6a). It is found that the ΔG_{H^*} value of the NiS_2/MoS_2 composite is very close to zero, which is the thermodynamic limit value [46]. This further suggests and confirms the enhanced HER performance of NiS_2/MoS_2/RGO composites. The enhanced HER activity of NiS_2/MoS_2/RGO catalyst may be due to H interacting with S at the heterointerfaces of NiS_2 and MoS_2 phases, where H^+ is adsorbed. The H^+ absorption energy of the NiS_2 nanoparticles, MoS_2 nanosheets, and NiS_2/MoS_2 composite are -1.57, -0.51, and -0.30 eV, respectively. The NiS_2/MoS_2/RGO composite offers relatively weak attractive forces for proton and H* easily desorbed from the surface of the catalyst. Basically, interchange transfer creates a local dipole at the interface of NiS_2/MoS_2/RGO composite that consequently reduces the work function and improves its catalytic activity and stability. So, the ideal ΔG_{H^*} of hydrogen adsorption over NiS_2/MoS_2/RGO composite is due to minimum work function (3.98 eV). On the other hand, the simulated work function of pristine MoS_2 and NiS_2 are 3.50 and 4.62 eV, respectively. This effect can be further viewed from the electron difference density (EDD) distribution Fig. 6b and Fig. S8. In the case of MoS_2 and NiS_2 systems, the proton is strongly absorbed on MoS_2 nanosheets which is further stronger in NiS_2, which causes a hurdle

in the desorption of H* and leads to a lowers HER performance.

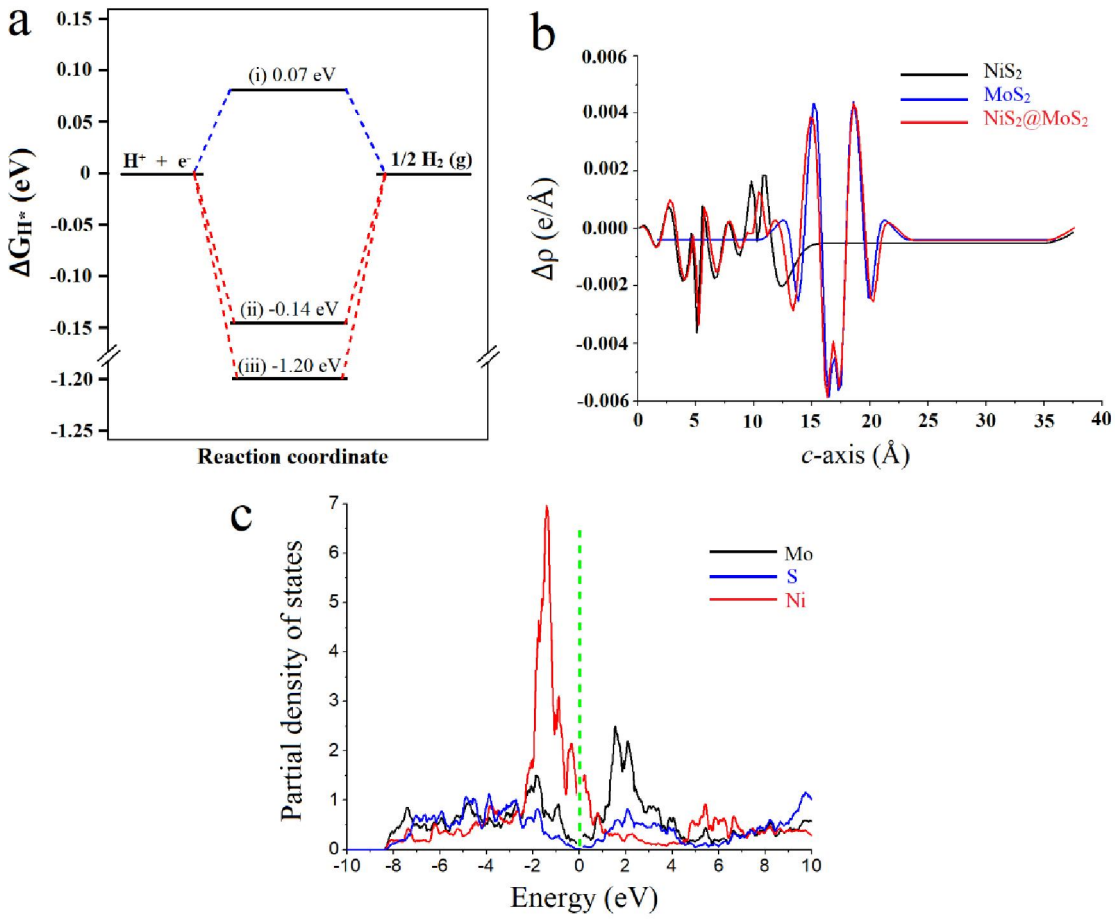

Fig. 6. (a) Energy diagram for the Gibbs free energy (ΔG_{H^*}) of HER process of NiS_2/MoS_2 (i), MoS_2 (ii), NiS_2 (iii), (b) EDD average electron density difference ($\Delta\rho$) in c-direction for NiS_2, MoS_2, and NiS_2/MoS_2 samples. (c) PDOS of NiS_2/MoS_2 and the Fermi energy is set to 0 eV.

Furthermore, the improved HER performance of NiS_2/MoS_2/RGO composite may be due to the strong interaction of NiS_2 and MoS_2 phases. The PDOS plot of NiS_2/MoS_2/RGO is given in Fig. 6c. Comprehensive analysis of Fig. 6c led us to conclude that occupied orbitals of Ni and Mo are mutually overlapped in the valence band (-10 to 0 eV) and unoccupied anti-bonding orbitals of Ni, Mo, and S are overlapped in the conduction band DOS (0 to 10 eV). These orbital overlapping show the charge transferring at the interface and the stability of

NiS_2/MoS_2/RGO catalysts.

In addition, RGO acts as a substrate and reduces the agglomeration of NiS_2/MoS_2 sphere. It can also maintain the good conductivity of NiS_2/MoS_2/RGO composites for improved electrocatalytic HER performances.

4. Conclusions

In summary, we have synthesized hierarchical spheres of NiS_2/MoS_2/RGO composite using the hydrothermal method. The NiS_2/MoS_2/RGO-9 catalyst shows excellent activity with an overpotential of 136 mV at a current density of 10 mA cm^{-2}, a small Tafel slope of 53.4 mV $dec^{-1,}$ and stability in acid solution. We found that the enhanced HER performance of NiS_2/MoS_2/RGO catalyst is due to the synergistic effect of bimetallic sulfide that provides abundant heterointerface as an active site. The RGO provides a conductive channel and prevents aggregation of NiS_2/MoS_2 spheres. In order to validate and confirm the HER activity and stability of NiS_2/MoS_2/RGO catalyst, Theoretical calculations confirm that heterointerface facilitates the HER process on NiS_2/MoS_2 catalyst by lowering Gibbs free energy (0.07 eV). Therefore, this work provides a simple method for combining bimetallic sulfides and carbon materials to synthesize high-efficiency catalysts with excellent performance under acidic conditions.

Acknowledgments: The support from the National Natural Science Foundation of China (No. 22150410332) and the start-up foundation for the introduction of talent at Jiangsu University of Science and Technology, China, are highly appreciated. We also acknowledge the University of Exeter's Advanced Research Computing facilities (Athena HPC Cluster) for carrying out the

DFT part and Prof. Xiaohong Li (Energy Storage Group) for the provision of QuantumATK_2019.12 software.

References

[1] Z. Chen, X. Duan, W. Wei, S. Wang, B.J. Ni, Recent advances in transition metal-based electrocatalysts for alkaline hydrogen evolution, J. Mater. Chem. A 7 (2019) 14971-15005. https://doi.org/10.1039/c9ta03220g.

[2] H. Ishaq, I. Dincer, Comparative assessment of renewable energy-based hydrogen production methods, Renew. Sust. Energ. Rev. 135 (2021) 110192. https://doi.org/10.1016/j.rser.2020.110192.

[3] C. Acar, I. Dincer, The potential role of hydrogen as a sustainable transportation fuel to combat global warming, Int. J. Hydrog. Energy 45 (2020) 3396-3406. https://doi.org/10.1016/j.ijhydene.2018.10.149.

[4] W. Wang, X. Xu, W. Zhou, Z. Shao, Recent progress in metal-organic frameworks for applications in electrocatalytic and photocatalytic water splitting, Adv. Sci. 4 (2017) 1600371. https://doi.org/10.1002/advs.201600371.

[5] S. A. Shah, X. Shen, A. Yuan, Z. Ji, X. Yue, G. Zhu, H. Zhou, K. Xu, J. Zhu, Y. Chen, One step in-situ synthesis of Ni_3S_2/Fe_2O_3/N-doped carbon composites on Ni foam as an efficient electrocatalyst for overall water splitting, Appl. Surf. Sci. 527 (2020) 146918. https://doi.org/10.1016/j.apsusc.2020.146918.

[6] L. Peng, C. Wang, Q. Wang, R. Shi, T. Zhang, G. I. N. Waterhouse, Rationally designed Ni–Ni_3S_2 interfaces for efficient overall water electrolysis, Adv. Energy Sustainability Res. 2 (2021) 2100078. https://doi.org/10.1002/aesr.202100078

[7] M. Tavakkoli, N. Holmberg, R. Kronberg, H. Jiang, J. Sainio, E.I. Kauppinen, T. Kallio, K. Laasonen, Electrochemical activation of single-walled carbon nanotubes with pseudo-atomic-scale platinum for the hydrogen evolution reaction, ACS Catal. 7 (2017) 3121-3130. https://doi.org/10.1021/acscatal.7b00199.

[8] W. Yaseen, M. Xie, B.A. Yusuf, Y.G. Xu, N. Ullah, M. Rafiq, A. Ali, J.M. Xie, Synergistically coupling of Co/Mo_2C/$Co_6Mo_6C_2$@C electrocatalyst for overall water splitting: The role of carbon precursors in structural engineering and catalytic activity, Appl. Surf. Sci. 579 (2022) 14. https://doi.org/10.1016/j.apsusc.2021.152148.

[9] Z. Zhuang, S.A. Giles, J. Zheng, G.R. Jenness, S. Caratzoulas, D.G. Vlachos, Y. Yan, Nickel supported on nitrogen-doped carbon nanotubes as hydrogen oxidation reaction catalyst in alkaline electrolyte, Nat Commun 7 (2016) 10141. https://doi.org/10.1038/ncomms10141.

[10] D.V. Esposito, S.T. Hunt, Y.C. Kimmel, J.G. Chen, A new class of electrocatalysts for hydrogen production from water electrolysis: metal monolayers supported on low-cost transition metal carbides, J. Am. Chem. Soc. 134 (2012) 3025-33. https://doi.org/10.1021/ja208656v.

[11] P. Xiao, W. Chen, X. Wang, A Review of Phosphide-based materials for electrocatalytic hydrogen evolution, Adv. Energy Mater. 5 (2015) 1500985. https://doi.org/10.1002/aenm.201500985.

[12] S.A. Shah, X. Shen, M. Xie, G. Zhu, Z. Ji, H. Zhou, K. Xu, X. Yue, A. Yuan, J. Zhu, Y. Chen, Nickel@Nitrogen-Doped Carbon@MoS_2 nanosheets: An efficient electrocatalyst for hydrogen evolution reaction, Small 15 (2019) 1804545. https://doi.org/10.1002/smll.201804545.

[13] L. Shanga, Y. Zhao, X. Yu. Kong, R. Shi, G. I. N. Waterhouse, L. Wen, T. Zhang, Underwater superaerophobic Ni nanoparticle-decorated nickel–molybdenum nitride nanowire arrays for hydrogen evolution in neutral media, Nano Energy 78 (2020) 105375. https://doi.org/10.1016/j.nanoen.2020.105375

[14] W. Yaseen, N. Ullah, M. Xie, W. Wei, Y.G. Xu, M. Zahid, C.J. Oluigbo, B.A. Yusuf, J.M. Xie, Cobalt-Iron nanoparticles encapsulated in mesoporous carbon nanosheets: A one-pot synthesis of highly stable electrocatalysts for overall water splitting, Int. J. Hydrog. Energy 46 (2021) 5234-5249. https://doi.org/10.1016/j.ijhydene.2020.11.041.

[15] H.W. Liang, S. Bruller, R. Dong, J. Zhang, X. Feng, K. Mullen, Molecular metal-N_x centres in porous carbon for electrocatalytic hydrogen evolution, Nat Commun 6 (2015) 7992. https://doi.org/10.1038/ncomms8992.

[16] I.H. Kwak, H.S. Im, D.M. Jang, Y.W. Kim, K. Park, Y.R. Lim, E.H. Cha, J. Park, $CoSe_2$ and $NiSe_2$ nanocrystals as superior bifunctional catalysts for electrochemical and photoelectrochemical water splitting, ACS Appl. Mater. Interfaces 8 (2016) 5327-5334. https://doi.org/10.1021/acsami.5b12093.

[17] W. Wang, L. Li, S. Tan, K. Wu, G. Zhu, Y. Liu, Y. Xu, Y. Yang, Preparation of NiS_2//MoS_2 catalysts by two-step hydrothermal method and their enhanced activity for hydrodeoxygenation of p-cresol, Fuel 179 (2016) 1-9. https://doi.org/10.1016/j.fuel.2016.03.068.

[18] Ali, P. K. Shen, Nonprecious metal's graphene-supported electrocatalysts for hydrogen evolution reaction: Fundamentals to application. Carbon Energy. 2 (2020) 99-121. https://doi.org/10.1002/cey2.26

[19] Y. Yan, B. Xia, Z. Xu, X. Wang, Recent development of Molybdenum sulfides as advanced

electrocatalysts for hydrogen evolution reaction, ACS Catal. 4 (2014) 1693-1705. https://doi.org/10.1021/cs500070x.

[20] W. Xiao, P. Liu, J. Zhang, W. Song, Y.P. Feng, D. Gao, J. Ding, Dual-functional N dopants in edges and basal plane of MoS_2 nanosheets toward efficient and durable hydrogen evolution, Adv. Energy Mater. 7 (2017) 1602086. https://doi.org/10.1002/aenm.201602086.

[21] J.E. ten Elshof, H. Yuan, P. Gonzalez Rodriguez, Two-dimensional metal oxide and metal hydroxide nanosheets: synthesis, controlled assembly and applications in energy conversion and storage, Adv. Energy Mater. 6 (2016) 1600355. https://doi.org/10.1002/aenm.201600355.

[22] T.F. Jaramillo, K.P. Jorgensen, J. Bonde, J.H. Nielsen, S. Horch, I. Chorkendorff, Identification of active edge sites for electrochemical H_2 evolution from MoS_2 nanocatalysts, Science 317 (2007) 100-2. https://doi.org/10.1126/science.1141483.

[23] M. Chatti, T. Gengenbach, R. King, L. Spiccia, A.N. Simonov, Vertically aligned interlayer expanded MoS_2 nanosheets on a carbon support for hydrogen evolution Electrocatalysis, Chem. Mater. 29 (2017) 3092-3099. https://doi.org/10.1021/acs.chemmater.7b00114.

[24] J.-T. Ren, L. Chen, D.-D. Yang, Z.-Y. Yuan, Molybdenum-based nanoparticles (Mo_2C, MoP and MoS_2) coupled heteroatoms-doped carbon nanosheets for efficient hydrogen evolution reaction, Appl. Catal. B 263 (2020). https://doi.org/10.1016/j.apcatb.2019.118352.

[25] H. Li, C. Tsai, A.L. Koh, L. Cai, A.W. Contryman, A.H. Fragapane, J. Zhao, H.S. Han, H.C. Manoharan, F. Abild-Pedersen, J.K. Norskov, X. Zheng, Activating and optimizing MoS_2 basal planes for hydrogen evolution through the formation of strained sulphur vacancies, Nat. Mater. 15 (2016) 48-53. https://doi.org/10.1038/nmat4465.

[26] K.D. Rasamani, F. Alimohammadi, Y. Sun, Interlayer-expanded MoS_2, Mater. Today 20

(2017) 83-91. https://doi.org/10.1016/j.mattod.2016.10.004.

[27] L. Yang, W. Zhou, J. Lu, D. Hou, Y. Ke, G. Li, Z. Tang, X. Kang, S. Chen, Hierarchical spheres constructed by defect-rich MoS_2/carbon nanosheets for efficient electrocatalytic hydrogen evolution, Nano Energy 22 (2016) 490-498. https://doi.org/10.1016/j.nanoen.2016.02.056.

[28] G. Ye, Y. Gong, J. Lin, B. Li, Y. He, S.T. Pantelides, W. Zhou, R. Vajtai, P.M. Ajayan, Defects engineered monolayer MoS_2 for improved hydrogen evolution reaction, Nano Lett. 16 (2016) 1097-103. https://doi.org/10.1021/acs.nanolett.5b04331.

[29] J. Xie, J. Zhang, S. Li, F. Grote, X. Zhang, H. Zhang, R. Wang, Y. Lei, B. Pan, Y. Xie, Controllable disorder engineering in oxygen-incorporated MoS_2 ultrathin nanosheets for efficient hydrogen evolution, J. Am. Chem. Soc. 135 (2013) 17881-8. https://doi.org/10.1021/ja408329q.

[30] Y. Liu, S. Jiang, S. Li, L. Zhou, Z. Li, J. Li, M. Shao, Interface engineering of (Ni, Fe)S_2@MoS_2 heterostructures for synergetic electrochemical water splitting, Appl. Catal. B 247 (2019) 107-114. https://doi.org/10.1016/j.apcatb.2019.01.094.

[31] J.G. Hou, B. Zhang, Z.W. Li, S.Y. Cao, Y.Q. Sun, Y.Z. Wu, Z.M. Gao, L.C. Sun, Vertically aligned oxygenated-CoS_2-MoS_2 heteronanosheet architecture from polyoxometalate for efficient and stable overall water splitting, ACS Catal. 8 (2018) 4612-4621. https://doi.org/10.1021/acscatal.8b00668.

[32] Z.F. Huang, J.J. Song, K. Li, M. Tahir, Y.T. Wang, L. Pan, L. Wang, X.W. Zhang, J.J. Zou, Hollow cobalt-based Bimetallic sulfide polyhedra for efficient all-pH-value electrochemical and photocatalytic hydrogen evolution, J. Am. Chem. Soc. 138(4) (2016) 1359-1365.

https://doi.org/10.1021/jacs.5b11986.

[33] H. Khan, S.A. Shah, W.u. Rehman, F. Chen, CoS_2 Nanoparticles-decorated MoS_2/rGO nanosheets as an efficient electrocatalyst for ultrafast hydrogen evolution, Adv. Mater. Interfaces 9 (2021) 2101294. https://doi.org/10.1002/admi.202101294.

[34] Z.K. Shi, Z.B. Yu, J. Guo, R.H. Jiang, Y.P. Hou, Y.S. Chen, H.L. Chen, M. Wang, H. Pang, W.J. Tang, Lattice distortion of crystalline-amorphous nickel molybdenum sulfide nanosheets for high-efficiency overall water splitting: libraries of lone pairs of electrons and in situ surface reconstitution, Nanoscale, 14 (2022) 1370-1379. https://doi.org/10.1039/d1nr07438e.

[35] H. Mao, X. Guo, Q. Fan, Y. Fu, H. Yang, D. Liu, S. Wu, Q. Wu, X.-M. Song, Improved hydrogen evolution activity by unique NiS_2-MoS_2 heterostructures with misfit lattices supported on poly(ionic liquid)s functionalized polypyrrole/graphene oxide nanosheets, Chem. Eng. J. 404 (2021) 126253. https://doi.org/10.1016/j.cej.2020.126253.

[36] L. Wang, T. Guo, S. Sun, Y. Wang, X. Chen, K. Zhang, D. Zhang, Z. Xue, X. Zhou, Tree-Like NiS_2/MoS_2-RGO Nanocomposites as pH universal electrocatalysts for hydrogen evolution reaction, Catal. Lett. 149 (2019) 1197-1210. https://doi.org/10.1007/s10562-019-02698-7

[37] Y. Zheng, J. Rong, J. Xu, Y. Zhu, T. Zhang, D. Yang, F. Qiu, Accessible active sites activated by cobalt-doping into MoS_2/NiS_2 nanosheet array electrocatalyst for enhanced hydrogen evolution reaction, Appl. Surf. Sci. 563 (2021) 150385. https://doi.org/10.1016/j.apsusc.2021.150385.

[38] C. Li, M. Liu, H. Ding, L. He, E. Wang, B. Wang, S. Fan, K. Liu, A lightly Fe-doped (NiS_2/MoS_2)/carbon nanotube hybrid electrocatalyst film with laser-drilled micropores for

stabilized overall water splitting and pH-universal hydrogen evolution reaction, J. Mater. Chem. A 8(34) (2020) 17527-17536. https://doi.org/10.1039/d0ta04586a.

[39] W. S. Hummers, R. E. Offeman, Preparation of Graphitic Oxide, J. Am. Chem. Soc. 80 (1958) 1339–1339. https://doi.org/10.1021/ja01539a017.

[40] X. Cai, X. Shen, L. Ma, Z. Ji, C. Xu, A. Yuan, Solvothermal synthesis of NiCo-layered double hydroxide nanosheets decorated on RGO sheets for high performance supercapacitor, Chem. Eng. J. 268 (2015) 251-259. https://doi.org/10.1016/j.cej.2015.01.072.

[41] Q. Gao, S. Wang, H. Fang, J. Weng, Y. Zhang, J. Mao, Y. Tang, One-dimensional growth of MoO_x-based organic-inorganic hybrid nanowires with tunable photochromic properties, J. Mater. Chem. A 22 (2012) 4709-4715. https://doi.org/10.1039/c2jm15443a.

[42] Atomistix Tool Kit version 2019.12, Quantum Wise A/S (www.quantumwise.com).

[43] VirtualNanoLab version 2019.12, QuantumWise A/S (www.quantumwise.com).

[44] G. Kresse, D. Joubert From ultrasoft pseudopotentials to the projector augmented-wave method Phys. Rev. B, 59 (1999), 1758. https://doi.org/10.1103/PhysRevB.59.1758.

[45] S. A. Shah, L. Xu, R. Sayyar, T. Bian, Z. Liu, A. Yuan, X. Shen, I. Khan, A. Ali Tahir, H. Ullah, Growth of MoS_2 nanosheets on M@N-doped carbon particles (M = Co, Fe or CoFe Alloy) as an efficient electrocatalyst toward hydrogen evolution reaction, Chem. Eng. J. 428 (2022) 132126. https://doi.org/10.1016/j.cej.2021.132126.

[46] Nørskov, T. Bligaard, A. Logadottir, J. Kitchin, J.G. Chen, S. Pandelov, U. Stimming Trends in the exchange current for hydrogen evolution, J. Electrochem. Soc., 152 (2005), J23. https://doi.org/10.1149/1.1856988

[47] M.W. Chase, NIST-JANAF thermochemical tables for oxygen fluorides, J. Phys. Chem.

Ref. Data, 25 (1996) 551-603. https://doi.org/10.1063/1.555992

[48] Z.H. Deng, L. Li, W. Ding, K. Xiong, Z.D. Wei, Synthesized ultrathin MoS_2 nanosheets perpendicular to graphene for catalysis of hydrogen evolution reaction, Chem. Commun. 51 (2015) 1893-6. https://doi.org/10.1039/c4cc08491h.

[49] S.A. Shah, G. Zhu, X. Shen, L. Kong, Z. Ji, K. Xu, H. Zhou, J. Zhu, P. Song, C. Song, A. Yuan, X. Miao, Controllable sandwiching of reduced rraphene oxide in hierarchical defect-rich MoS_2 ultrathin nanosheets with expanded interlayer spacing for electrocatalytic hydrogen evolution reaction, Adv. Mater. Interfaces 5 (2018) 1801093. https://doi.org/10.1002/admi.201801093.

[50] Y.J. Tang, Y. Wang, X.L. Wang, S.L. Li, W. Huang, L.Z. Dong, C.H. Liu, Y.F. Li, Y.Q. Lan, Molybdenum disulfide/nitrogen-doped reduced graphene oxide nanocomposite with enlarged interlayer spacing for electrocatalytic hydrogen evolution, Adv. Energy Mater. 6 (2016) 1600116. https://doi.org/10.1002/aenm.201600116.

[51] Z. Deng, H. Jiang, Y. Hu, Y. Liu, L. Zhang, H. Liu, C. Li, 3D Ordered Macroporous MoS_2@C Nanostructure for Flexible Li-ion batteries, Adv. Mater. 29(10) (2017) 1603020. https://doi.org/10.1002/adma.201603020.

[52] J. Wang, Z. Liu, C. Zhan, K. Zhang, X. Lai, J. Tu, Y. Cao, 3D hierarchical NiS_2/MoS_2 nanostructures on CFP with enhanced electrocatalytic activity for hydrogen evolution reaction, J. Mater. Sci. 39 (2020) 155-160. https://doi.org/10.1016/j.jmst.2019.05.037.

[53] X. Yang, J. Mao, H. Niu, Q. Wang, K. Zhu, K. Ye, G. Wang, D. Cao, J. Yan, NiS_2/MoS_2 mixed phases with abundant active edge sites induced by sulfidation and graphene introduction towards high-rate supercapacitors, Chem. Eng. J. 406 (2021) 126713.

https://doi.org/10.1016/j.cej.2020.126713.

[54] L. Xu, S. A. Shah, H. Khan, R. Sayyar, X. Shen, I. Khan, A. Yuan, W. Yaseen, Z. A.Ghazi, A. Naeem, H. Ullah, X. Li, C. Wang, Ni3S2 nanostrips@FeNi-$NiFe_2O_4$ nanoparticles embedded in N-doped carbon microsphere: An improved electrocatalyst for oxygen evolution reaction. J. Colloid Interface Sci. 617 (2022) 1-10. https://doi.org/10.1016/j.jcis.2022.02.129.

[55] T. An, Y. Wang, J. Tang, W. Wei, X. Cui, A.M. Alenizi, L. Zhang, G. Zheng, Interlaced NiS_2–MoS_2 nanoflake-nanowires as efficient hydrogen evolution electrocatalysts in basic solutions, J. Mater. Chem. A 4 (2016) 13439-13443. https://doi.org/10.1039/c6ta05022k.

[56] G. Zhu, X. Xie, Y. Liu, X. Li, K. Xu, X. Shen, Y. Yao, S. A. Shah. Fe_3O_4@NiS_x/rGO composites with amounts of heterointerfaces and enhanced electrocatalytic properties for oxygen evolution, Appl. Surf. Sci. 442 (2018) 256-263.

https://doi.org/10.1016/j.apsusc.2018.02.097.

[57] Y. Li, H. Wang, L. Xie, Y. Liang, G. Hong, H. Dai, MoS_2 nanoparticles grown on graphene: an advanced catalyst for the hydrogen evolution reaction, J. Am. Chem. Soc. 133 (2011) 7296-9. https://doi.org/10.1021/ja201269b.